Microfluid Nanofluid (2012) 12:485–498
DOI 10.1007/s10404-011-0890-6

RESEARCH PAPER

Microfluidic systems for the analysis of viscoelastic fluid flow phenomena in porous media

F. J. Galindo-Rosales · L. Campo-Deaño · F. T. Pinho · E. van Bokhorst · P. J. Hamersma · M. S. N. Oliveira · M. A. Alves

Received: 22 March 2011 / Accepted: 27 September 2011 / Published online: 22 October 2011

Abstract In this study, two microfluidic devices are proposed as simplified 1-D microfluidic analogues of a porous medium. The objectives are twofold: firstly to assess the usefulness of the microchannels to mimic the porous medium in a controlled and simplified manner, and secondly to obtain a better insight about the flow characteristics of viscoelastic fluids flowing through a packed bed. For these purposes, flow visualizations and pressure drop measurements are conducted with Newtonian and viscoelastic fluids. The 1-D microfluidic analogues of porous medium consisted of microchannels with a sequence of contractions/expansions disposed in symmetric and asymmetric arrangements. The real porous medium is in reality, a complex combination of the two arrangements of particles simulated with the microchannels, which can be considered as limiting ideal configurations. The results show that both configurations are able to mimic well the pressure drop variation with flow rate for Newtonian fluids. However, due to the intrinsic differences in the deformation rate profiles associated with each microgeometry, the symmetric configuration is more suitable for studying the flow of viscoelastic fluids at low *De* values, while the asymmetric configuration provides better results at high *De* values. In this way, both microgeometries seem to be complementary and could be interesting tools to obtain a better insight about the flow of viscoelastic fluids through a porous medium. Such model systems could be very interesting to use in polymer-flood processes for enhanced oil recovery, for instance, as a tool for selecting the most suitable viscoelastic fluid to be used in a specific formation. The selection of the fluid properties of a detergent for cleaning oil contaminated soil, sand, and in general, any porous material, is another possible application.

Keywords Microfluidics · Porous media · Rheology · Contraction-expansion · Viscoelastic fluids

1 Introduction

It is well known that some additives impart non-Newtonian fluid properties to aqueous and hydrocarbon systems, which have been widely used in applications related to the petroleum industry, among others (Gaitonde and Middleman 1966; Marshall and Metzner 1967; Wissler 1971). These additives are used in polymer-flood processes for enhanced oil recovery and show the practical relevance of investigating non-Newtonian fluid flow through porous media. The high price of oil and the need for increasingly higher rates of recovery foster the use of such advanced recovery techniques (Taylor and Nasr-El-Din, 1998). In addition to enhanced oil recovery, non-Newtonian fluid flow through porous media is relevant in a variety of applications, such as in polymer processing, lubrication and waste disposal applications (Chhabra et al. 2001).

F. J. Galindo-Rosales (✉) · E. van Bokhorst · M. S. N. Oliveira · M. A. Alves
Centro de Estudos de Fenómenos de Transporte (CEFT), Departamento de Engenharia Química, Faculdade de Engenharia da Universidade do Porto, R. Dr. Roberto Frias, 4200-465 Porto, Portugal
e-mail: galindo@fe.up.pt; curro@galindorosales.com

L. Campo-Deaño · F. T. Pinho
Centro de Estudos de Fenómenos de Transporte (CEFT), Departamento de Engenharia Mecânica, Faculdade de Engenharia da Universidade do Porto, R. Dr. Roberto Frias, 4200-465 Porto, Portugal

E. van Bokhorst · P. J. Hamersma
Department of Chemical Engineering, Delft University of Technology, Julianalaan 136, 2628 BL Delft, The Netherlands

Non-Newtonian is a generic term that incorporates a variety of complex fluid phenomena, which requires sophisticated mathematical models for proper description. Further complications arise when considering the flow through porous media, due to the complexity of the flow paths, which include the coexistence of shear and extensional components. So far, no general methodology has been developed. In the absence of such a general approach, four main models are found in the literature to deal with the flow of complex fluids in porous media, namely continuum models, "bundle of tubes" models, pore-scale network modeling and numerical methods (Sochi 2010).

1. The *continuum models* are widely used and they represent a simplified macroscopic approach in which the porous medium is treated as a continuum. All the complexities and fine details of the microscopic pore structure are absorbed into bulk terms of correlations or of properties that reflect average properties of the medium, like permeability or porosity. Semi-empirical equations relating flow rate and pressure gradient such as Ergun's equation, Darcy's law or Carman–Kozeny's equation fall into this category. These empirical approaches are backed by years of experimental validation, and work well for Newtonian fluid flow (Balhoff and Thompson 2004). Regarding non-Newtonian flow, Pearson and Tardy (2002) reviewed the main continuum models used for describing transport in porous media with special emphasis on the effects of non-Newtonian rheology and concluded that none of the available continuum models gives accurate estimates of macroscopic transport properties (López 2004).
2. In the *capillary bundle models*, the flow channels in a porous medium are depicted as a bundle of tubes. The simplest form is the model with straight, cylindrical, identical parallel tubes oriented in a single direction. This model is only adequate for relatively simple unconsolidated and highly permeable porous media, whereas for more compact media more complex geometrical descriptions become necessary. Although simple, the capillary bundle approach does not allow for a correct interpretation of the flow of polymer solutions at the pore scale (Christopher and Middleman 1965; Sorbie et al. 1989), presumably because it only considers shear effects and is not able to incorporate extensional-flow effects, which become quite relevant whenever the fluid is elastic. In contrast, the response of a Newtonian fluid in extensional flow has a constant proportionality to that in shear flow for the same equivalent deformation rate.
3. *Pore-scale network modeling* is a relatively novel method that has been developed to deal with the flow through porous media and other related issues. It is a mesoscale method that partly accounts for the physics of flow and void space structure at pore level with affordable computational resources. The void space is described as a network of flow channels with idealized geometry. Rules that determine the transport properties in these channels are incorporated into the network to compute effective properties on a mesoscopic scale. The appropriate pore-scale averaged physics combined with a representative description of the pore space gives rise to models that can successfully predict the average flow behavior (Blunt 2001). The general strategy in network modeling is to use the rheology of the fluid and the void space description of the porous medium as an input to the model. The flow simulation in a network starts by modeling the flow in a single capillary and is subsequently extended to the network of capillaries, represented by a set of equations and satisfying mass conservation and momentum balance, which are solved simultaneously to find the pressure field and other relevant physical quantities (Sochi 2007).
4. *Numerical methods* are used to solve the flow field governing equations. This approach consists of a detailed description of the porous medium and the relevant physics at pore-scale level. The major advantage is the capability, in principle at least, to deal with time-dependent flows and complex geometrical configurations. The disadvantage is that the detailed pore space description is often complex, hard to implement and leads to large computational costs and serious convergence difficulties, the latter being enhanced for viscoelastic fluids. For these reasons, the flow processes and porous media currently within the reach of numerical investigation are restricted to the simplest ones (Sochi 2010; Liu and Wu 2009), unless very advanced computational resources are available.

Considering this scenario, it can be said that the problem of the flow of non-Newtonian fluids through porous media has been extensively analyzed over the past 50 years, although it is far from being fully understood.

A variety of porous media have been used in flow studies involving complex fluids. Included are models of porous media such as sand beds and matrices of uniformly packed spheres and woven screen, as well as alandum plugs, sandstone cores, porous metal disk, sintered glasses, and compressed glass wool. Each sample of a model of porous medium is in itself somewhat unique in geometric morphology, and there are formidable problems in precisely defining the flow conditions existing within any particular structure. Several of the published investigations concerned with more fundamental aspects of the flow of

non-Newtonian fluids through porous media involved the use of unconsolidated models (Savins 1969). For developing this study, we also used an unconsolidated packed bed of sand as a porous medium.

Viscoelasticity is one of the main features of non-Newtonian behavior exhibited by fluids made from polymer macromolecules. Apart from exhibiting shear-thinning behavior (the exception are Boger fluids), viscoelastic solutions also possess fading memory (Macosko 1994), the elongational viscosity is both strain and strain rate dependent (Petrie, 2006a, b) and in some cases largely exceeds the shear viscosity. In particular, the strain hardening behavior of the Trouton ratio (the ratio between extensional and shear viscosities) complicates substantially the analysis of viscoelastic fluid flow through a porous medium and so it is not surprising that there is little definitive and quantitative information available on the role of viscoelasticity in the flow through porous media (Chhabra et al. 2001). It is the major aim of this study to contribute for an insight on this matter. To do it, dilute aqueous solutions of polyacrylamide (PAA) were used as model viscoelastic fluids. Moreover, polyacrylamide is an important polymer used for oil recovery applications, due to the pronounced elastic behavior and significant strain hardening behavior (Duda et al. 1983).

It is widely accepted that in porous media the converging–diverging nature of the flow paths brings out the influence of both extensional and shear properties of the fluid. The principal mode of deformation to which a material element is subjected as the flow converges into a constriction involves both shearing of the material element and stretching or elongation in the direction of the flow, while in the diverging portion the flow involves both shearing and compression or deceleration. The actual channel geometry determines the ratio of shearing to extensional contributions. Strong experimental evidence indicates that the flow of viscoelastic fluids through packed beds can exhibit significant increases in the pressure gradient with increasing flow rate, or an increase in the apparent viscosity, above that expected for purely viscous fluids with a similar shear viscosity. This increase has been linked with the strain hardening behavior of the fluid, coupled with the extensional nature of the flow field within the pores due to the successive expansions and contractions that a fluid element experiences as it flows through the medium (Metzner and Metzner 1970). Even though the flow field at pore level is not an ideal extensional flow, due to the simultaneous presence of shear and rotation, the increase in flow resistance is normally referred to as an extension thickening effect, though its precise nature is yet unknown or controversial (Sochi 2009).

Microfluidics is the science and technology of systems that processes or manipulates very small amounts of fluid by using channels with characteristic length-scales of about or less than 100 μm (Whitesides 2006). The numerous advantages of microfluidics, namely the reduced amounts of sample and reagents needed, the high surface-to-volume ratio, the substantial waste reduction, the low cost of fabrication and the possibility of producing highly integrated and disposable devices, have stimulated remarkable interest and unraveled an extensive range of applications (Oliveira et al. 2008). Moreover, some microfluidic devices also offer the advantage of having optical access to analyze the flow using non-intrusive optical techniques (Devasenathipathy et al. 2003; Sinton 2004). For instance, it is possible to quantify the velocity field in various planes of the microchannel by means of microparticle image velocimetry (μPIV) (Santiago et al. 1998; Oliveira et al. 2007), as well as using fluorescence microscopy to visualize the flow patterns and measure the speed of the flow (Stone et al. 2004).

The pore space within a porous medium is not only difficult to access visually but also often characterized by parameters like connectivity and tortuosity, which are difficult to measure and quantify. As materials like sand and clay have an average particle size on the order of hundred microns, microchannels containing a series of contractions and expansions could be used as simple porous medium analogues. In this work, microfluidic devices with two different geometries are proposed as simplified 1-D microfluidic analogues for a porous medium. We pursue two main aims with this work: firstly, to validate the usefulness of these microfluidic channels to mimic a real porous medium; secondly, to analyze the flow of a dilute polymer solution through the microchannels to explain the results obtained with the real porous medium. This analysis will be based on experiments involving flow visualizations, pressure drop and flow rate measurements, as well as rheological characterization of the fluids before and after flowing through the porous medium.

2 Materials and methods

2.1 Materials

In this study, we used a Newtonian liquid (de-ionized water) and two dilute aqueous solutions of polyacrylamide ($M_w = 18 \times 10^6 g/mol$, supplied by Sigma-Aldrich Co.) at 50 and 125 ppm by weight, hereafter named as PAA50 and PAA125, respectively. These concentrations are well below the overlap concentration ($c^* = 512$ ppm) (Sousa et al. 2010). Solutions were prepared by mixing the polymer into the solvent (de-ionized water) at different concentrations, utilizing magnetic stirrers at low angular speed to avoid mechanical degradation of the polymer molecules. To prevent chemical degradation, all solutions were kept in a refrigerator. The density of all fluids was measured at 20°C

using a calibrated 25 cm^3 pycnometer: $\rho_{water} = 998.0\,kg/m^3$, $\rho_{PAA50} = 998.0\,kg/m^3$ and $\rho_{PAA125} = 998.2\,kg/m^3$.

2.2 Rheological characterization

The rheological behavior of the solutions was characterized experimentally under steady simple shear and uniaxial extensional flows. All the rheological tests were carried out at 20.0 ± 0.1°C.

The steady shear tests were used to determine the dependence of the shear viscosity with shear rate in steady flow. The shear viscosity curves were obtained using a controlled stress rotational rheometer (Physica MCR 301, Anton Paar GmbH). Since the shear rates attained in a porous media can be very high, it is essential to have information at high shear rates. From a systematic experimental study about the adequacy of different geometries available (cone-plate, parallel plates and concentric cylinders) to accurately measure the shear viscosity of de-ionized water, we selected the parallel plates with a diameter of 50 mm and a gap of 0.1 mm which provided reliable measurements at high shear rates without significant effect of inertia-driven secondary flows. In addition, the sensitivity at low shear rates was very similar to that of the cone-plate geometry. All viscosity curves were measured for shear rates, $\dot{\gamma}$, ranging from 0.1 to 10,000 s^{-1} in 15 steps logarithmically distributed. Three independent runs were carried out to ensure the reproducibility of the measurements. Figure 1 shows that both solutions exhibit shear thinning behavior in the range of shear rates considered. Moreover, all the steady shear viscosity values measured are within the two reliable measurement limits, i.e. the minimum torque line (the line represented corresponds to 20 times the torque resolution of the rheometer) and the line indicating the onset of inertial instabilities (Sdougos et al. 1984).

A capillary break-up extensional rheometer (Haake CaBER-1, Thermo Fischer Scientific Inc.) was used to measure the relaxation time of the polymer solutions under extensional flow. These measurements were performed using circular plates with a diameter $D_p = 6\,mm$. The initial separation height was set to $h_i = 3.01\,mm$. The liquid bridge confined between the two plates was initially stretched as the top plate moved linearly $[-50 \le t\,(ms) \le 0]$ to a final height, $h_f = 12.03\,mm$. Subsequently, the stretched liquid filament thins in a process driven by the competing effects of viscoelastic and capillary forces. The time evolution of the normalized mean diameter (D/D_0) curves in the elasto-capillary thinning phase were fitted using an exponential decay function (Fig. 2) (Entov and Hinch 1997)

$$\frac{D}{D_0} = Ce^{\frac{-t}{3\lambda}}, \qquad (1)$$

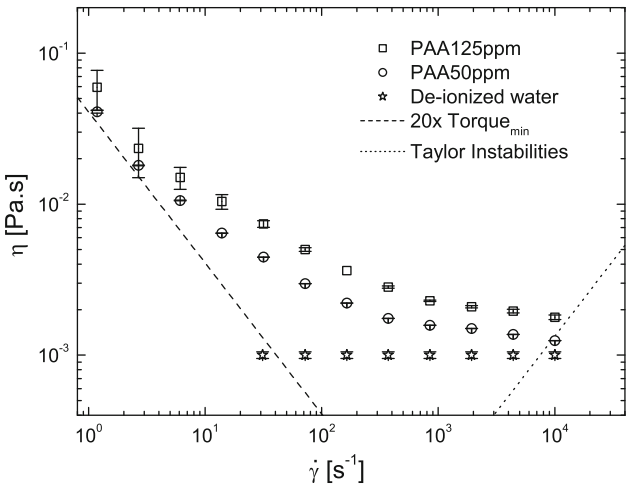

Fig. 1 Steady viscosity curve measured for the three working fluids at 20°C. The minimum measurable shear viscosity calculated from ×20 the minimum torque of the rheometer ($T_{min} = 10^{-7}\,N \cdot m$) and the line marking the onset of secondary flow due to Taylor instabilities are also shown as dashed and dotted lines, respectively

where D_0 is the initial diameter of the filament, C is a fluid dependent constant, t is the time and λ is the relaxation time. According to Campo-Deaño and Clasen (2010), the longest relaxation times of PAA solutions here considered can be accurately measured with the CaBER technique without any special protocol, given that the zero-shear viscosity of each viscoelastic fluid is sufficiently high (Fig. 1). Nevertheless, at least 20 independent runs were carried out for each fluid to ensure the reproducibility of the measurements. For quantitative purposes, in the calculation of the dimensionless numbers, we will use in all cases the relaxation time determined experimentally from

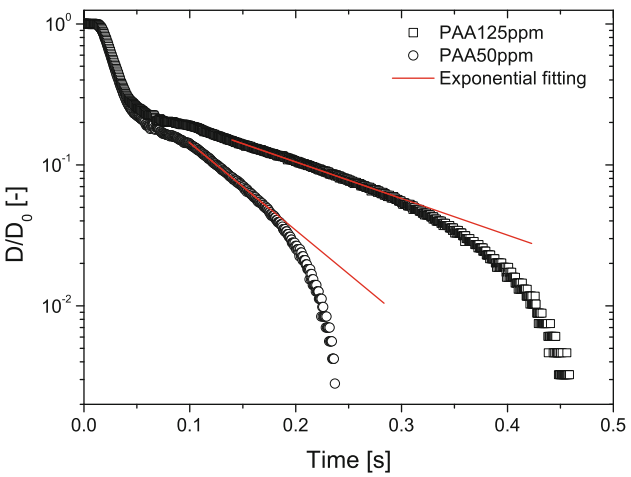

Fig. 2 Measurement of the longest relaxation time of the two PAA solutions with the capillary break-up extensional rheometer. Time evolution of the normalized diameters with corresponding exponential fittings at 20°C

the capillary break-up tests by means of Eq. 1: $\lambda_{PAA125} = 129 \pm 4$ ms and $\lambda_{PAA50} = 54 \pm 2$ ms.

2.3 Microchannels geometry, fabrication and experimental set-up

The complex nature of real porous media leads to the usage of a simplified and controlled representation of the porous structure to describe the phenomenological behavior of the medium. The model selection is a function of the desired level of detail, the intended application, the porous medium characteristics, such as the porosity, the particles type (shape, dimensions and internal structure), the medium type (consolidated or not), among other relevant properties. Since the macroscopic behavior depends on the local behavior at the level of the particles that compose the porous medium, any attempt to model it should be based on an adequate description of the local geometric and transport phenomena conditions. One-dimensional capillary networks can be viewed as networks of elements without intersections. Because of its simplicity, this was the first type of theoretical model to be proposed for modeling the porous media behavior, being the basis of the majority of correlations and equations currently used (Martins et al. 2009).

In this work, the porous medium is modeled as a bundle of non-uniform conduits with a periodic configuration. Both consist of a continuous series of contractions and expansions in two different arrangements: symmetric and asymmetric. Both geometries contain 117 repetitive elements and Fig. 3 shows a zoomed view of two sketches corresponding to these micro-geometries, where important dimensions are indicated, as well as their correspondence to the modeled arrangements of porous medium.

At the widest and narrowest parts, the widths of the microgeometries are W_1 and W_c, respectively, and the lengths of each element are L_1 and L_2. The depth of the channels (H) is uniform and was kept constant for both micro-devices studied. Table 1 summarizes the dimensions of the different microgeometries used in the experiments.

The flow behavior of Newtonian and non-Newtonian fluids was studied at room temperature (19.5 ± 0.9°C) for a wide range of flow rates, which were imposed using a syringe pump (PHD2000, Harvard Apparatus). Hamilton syringes with volumes ranging from 50 µl to 1 ml were used according to the desired flow rate and connected to the microchannels via Tygon tubing with 0.44 mm of internal diameter. The outlet of the microchannels was connected to Tygon tubing that directs the fluid to a reservoir open to the atmosphere where the fluid is collected.

Visualizations of the flow patterns relied on streak photography. For this purpose, the fluids were seeded with 1 µm fluorescent tracer particles (Nile Red, Molecular Probes, Invitrogen, Ex/Em: 520/580 nm). The optical set-up consists of an inverted epi-fluorescence microscope (Leica Microsystems GmbH, DMI 5000M) equipped with a CCD camera (Leica Microsystems GmbH, DFC350 FX), a filter cube (Leica Microsystems GmbH, excitation BP 530–545 nm, dichroic 565 nm, barrier filter 610–675 nm) and a 100 W mercury lamp light source. The microgeometries were continuously illuminated and pathline images were acquired using a $10\times$ $(\mathrm{NA} = 0.25)$ microscope objective (Leica Microsystems GmbH) and long exposure times ($\approx$ 1s) to obtain a visual fingerprint of the flow patterns in the focused center plane. The depth of field (DOF) for an optical system can be calculated as (Meinhart et al. 2000):

$$\delta_z = \frac{n\lambda_0}{(\mathrm{NA})} + \frac{ne}{(\mathrm{NA})M}, \quad (2)$$

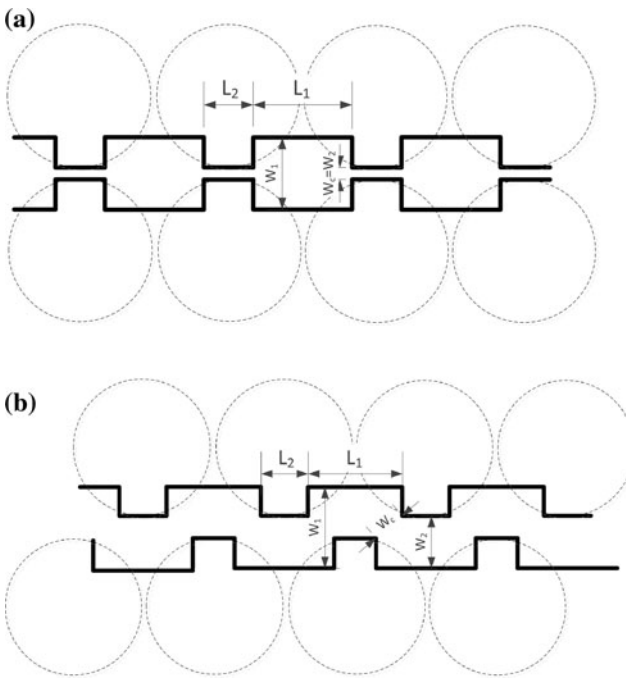

Fig. 3 Sketch of the two porous medium models (*dashed lines*) with the corresponding 1-D analogues of the microchannel geometry: **a** symmetric configuration; **b** asymmetric configuration. Table 1 provides the numerical values of the geometrical parameters

Table 1 Dimensions of microchannels used

Dimensions (µm)	Projected (chrome mask)		PDMS microchannels	
	Asymmetric	Symmetric	Asymmetric	Symmetric
W_1	100	100	108	108
W_2	66	33	72	40
W_c	46	33	52	40
H	100	100	103	103
L_1	100	100	106	106
L_2	33	33	31	31

where n is the refractive index, λ_0 is the wavelength of the light in vacuum, NA is the numerical aperture of the objective, e is the minimum detectable size and M is the total magnification. For our optical set-up, $e/M = 0.65$ μm, which is a value smaller than the tracer particle diameter, d_p, and $\delta_z = 12\mu m$, which amounts to 12% of the total channel depth.

The microchannels used in the experiments were fabricated in polydimethylsiloxane (PDMS) using standard soft lithography techniques (McDonald et al. 2000) and SU-8 photo-resist molds. PDMS elastomer has been widely used for the fabrication of microfluidic devices, because of its characteristics such as transparency, mechanical behavior, biocompatibility, rapid prototyping and low cost.

The pressure drop (ΔP) measurements were carried out by means of differential pressure sensors (Honeywell 26PC series). The pressure sensors were calibrated using a static column of water for pressures up to $\Delta P = 34$ kPa, and using a compressed air line and a manometer (Wika Instrument Corporation, model 332.50) with an accuracy of ±2 kPa for sensors that are able to measure higher pressure differences of up to 200 kPa. The ports of the pressure transducers were connected to two pressure taps, located upstream and downstream of the test section, containing the 117 repeating units. A 12V DC power supply (Lascar electronics, PSU 206) was used to power the pressure sensors that were also connected to a computer via a data acquisition card (NI USB-6218, National Instruments) to record the output data using LabView v7.1 software. The transient response of the pressure sensors was continuously recorded until steady-state was reached.

2.4 Packed bed column

2.4.1 Experimental set-up

The common procedure for studying flow in porous media is to measure pressure drop across a well-defined porous medium. Usually, a constant flow rate is imposed and manometers or pressure transducers are used to measure pressure differences (Duda et al. 1983). Consequently to compare the experimental results of a real porous medium with those of microfluidic analogs, we determined first the pressure drop as a function of the flow rate for the packed bed.

The experimental set-up for the packed bed column is shown in Fig. 4. It consists of a hollow acrylic cylindrical tube filled with unconsolidated sand. The internal diameter of the vertical cylinder is 2.0 ± 0.1 cm. The vertical alignment is checked with a bubble level before each measurement. The liquid was fed to the column from a pressurized reservoir and thus the inlet pressure could be varied and was measured with a manometer (Wika

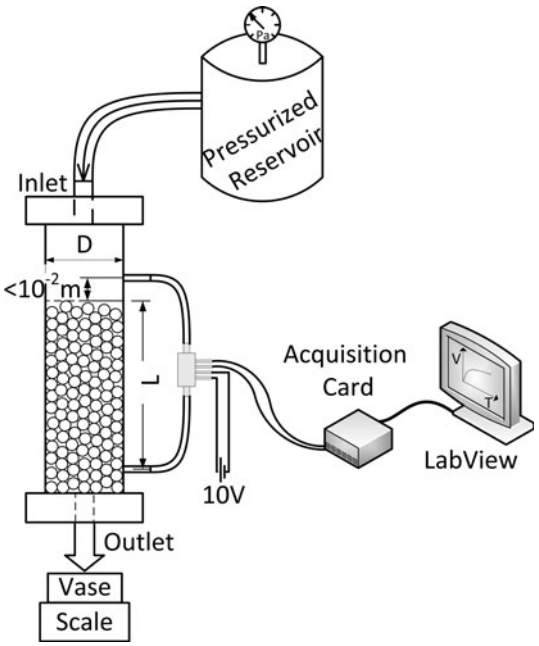

Fig. 4 Experimental set-up for measuring pressure losses of flows through a porous medium at different flow rates. Drawings are not to scale

Instrument Corporation, model 332.50). To avoid the fluidization of the bed, the flow inlet was placed at the top of the column and the outlet was located at the bottom part, where the fluid was collected and weighed along time, in a weighing scale with a resolution of ±0.01 g. The steady volumetric flow rate was calculated from the measured averaged mass flow rate and the density of the fluid. The pressure drop measurements were carried out between two pressure taps in the column separated by a distance of 14.7 ± 0.1 cm using differential pressure sensors (Honeywell 26PC series) covering values up to $\Delta P = 200$ kPa and a data acquisition system, as described in Sect. 2.3 for pressure drop measurements in microchannels.

Before each set of experiments and for each fluid, it is essential to ensure that the sand bed possesses the same porosity. This is achieved by loading exactly the same mass of sand to the acrylic tube and by measuring the same height of column sand $(14.7 \pm 0.1\ \text{cm})$, which guarantees that the same sand compaction was reached. Additionally, it was also checked using de-ionized water that the sand exhibited the same dependence of the pressure gradient with flow rate. New and clean sand was inserted in the column before each set of experiments to avoid the presence of any polymer residues in the sand from previous tests. Moreover, to ensure accurate pressure drop measurements, it has been verified that there were no air bubbles in any part of the set-up during the experimental runs.

We intentionally avoided the use of regulating valves in the experimental set-up to avoid any unnecessary degradation of the polymer chains beyond that already produced as the fluid flows through the porous medium. The degradation of the polymer chains due to the presence of elements in the set-up could eventually lead to a modification of the rheology of the fluid, and subsequently to a modification in the pressure drop measurements. Moreover, the collected fluid samples were rheologically characterized in simple shear and uniaxial elongational flows at the end of its single passage through the porous medium and compared with the corresponding rheology of the fresh sample.

The upper left insets in the two plots of Fig. 5 show that the steady shear viscosity of the fluids collected at the exit of the column did not suffer any significant modification from the original fresh sample data. However, the results of the measurements with CaBER (insets at lower right corner) show a decrease in the relaxation time for all solutions and cases, especially for those pertaining to higher flow rates (Table 2). This is a consequence of the molecules being stretched and partly broken (especially at higher flow rates) during the strong extensional flow through the porous medium. This effect is more visible in the PAA50 fluid, therefore a less concentrated solution is apparently more sensitive to modification in the molecular structure than more concentrated solutions. According to Rodd et al. (2005), as polymer concentration increases, the mobility of individual polymer chains is hindered through chain–chain interactions, resulting in anisotropic drag on the chains and/or an overall reduction in the finite extensibility of the polymer molecules. Thus, in the case of PAA125 fluid the higher concentration of polymer chains increases their interaction, and the consequent reduction of extensibility will lead to a less significant variation of the measured relaxation time.

2.4.2 *Determination of the sand particle size*

The effective particle size of sand in the porous medium was determined, by comparison with the results obtained in the microchannels, assuming in both cases similar variation of pressure gradient with interstitial velocity. First, the pressure gradient of de-ionized water flowing through the microchannels was measured as a function of the flow rate, and as expected for a Newtonian fluid, its pressure gradient along the microchannels varies linearly with the flow rate under laminar flow conditions, as shown in Fig. 6. Given the equivalent dimensions of both microchannels and the purely viscous behavior of water, both curves represented in Fig. 6, corresponding to different configurations (symmetric and asymmetric), nearly overlap. For the microchannels, the velocity was determined in the narrow parts

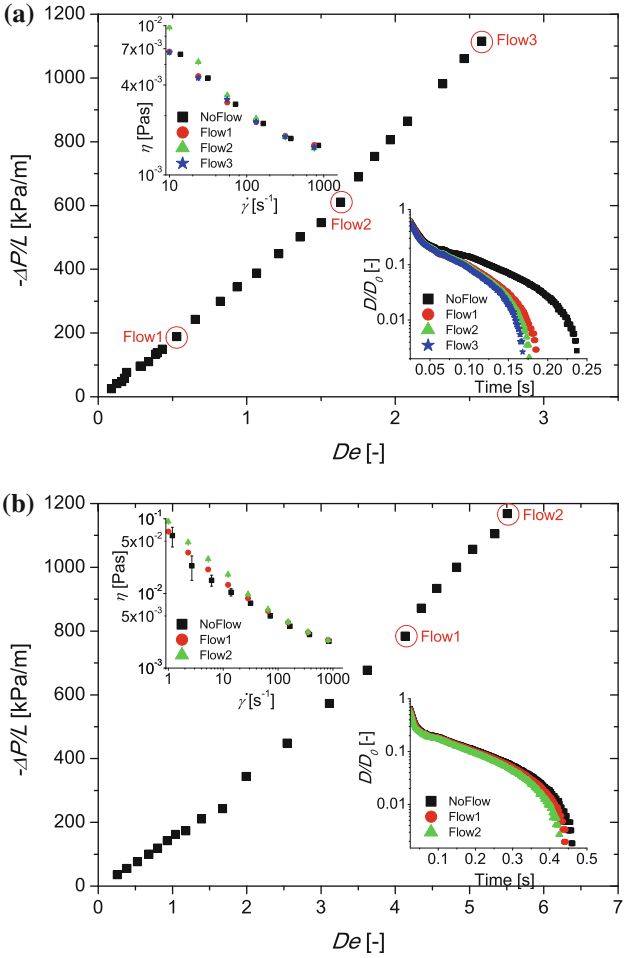

Fig. 5 Pressure gradient as a function of the Deborah number for the flow of the viscoelastic fluids through the porous medium. Inset graphs show the rheological properties of the samples collected at the exit of the porous medium at different flow rates: **a** PAA50; **b** PAA125

Table 2 Longest relaxation times measured with CaBER of PAA solutions after flowing through the porous medium at different flow rates, and comparison with fresh samples ("No flow")

Flow	PAA50 ppm		PAA125 ppm	
	U_i (m/s)	λ (ms)	U_i (m/s)	λ (ms)
No flow	0	54	0	129
Flow 1	0.004	37	0.013	123
Flow 2	0.013	35	0.017	118
Flow 3	0.019	34	–	–

The flow conditions are those illustrated in Fig. 5

of the geometries (width W_c), therefore this velocity scale is representative of the interstitial velocity occurring in a porous medium.

The laminar flow of a Newtonian fluid through a porous medium obeys Darcy's law (Darcy 1856):

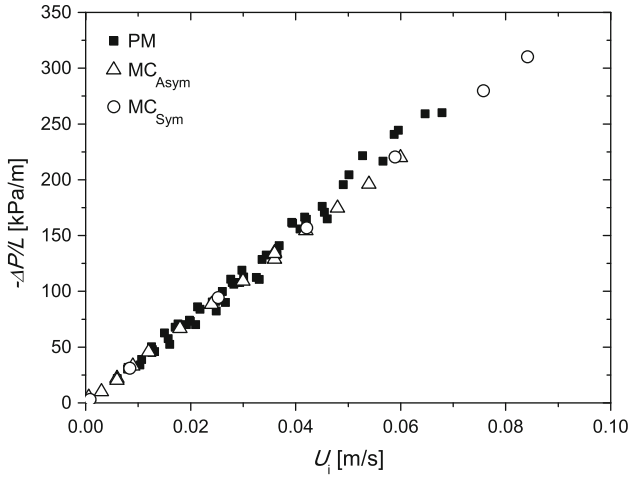

Fig. 6 Pressure gradient as a function of the interstitial velocity for the flow of a Newtonian fluid (de-ionized water) through the asymmetric (MC_{Asym}) and symmetric (MC_{Sym}) microchannels, and through the porous medium (PM)

$$U = \frac{k}{\mu}\left(\frac{-\Delta P}{L}\right), \tag{3}$$

where U is the superficial fluid velocity through the bed ($U = Q/A$, Q being the volumetric flow rate and A the cross-sectional area of the column), $-\Delta P$ is the frictional pressure drop across a bed of length L, μ represents the dynamic viscosity of the fluid, and k is the bed permeability, which is a measure of the bed flow resistance (inverse). We rewrite Eq. 3 as

$$\frac{-\Delta P}{L} = \frac{\mu}{k'}U_i, \tag{4}$$

to introduce the concept of modified permeability ($k' = k/\varepsilon$), based on the interstitial velocity ($U_i = U/\varepsilon$, with ε being the porosity of the porous medium), which is a more adequate description of the flow resistance in the microchannels, while still being useful in the context of porous media.

By fitting Eq. 4 to the experimental data set obtained with the microchannels, it is possible to calculate the modified permeability of the microchannels (k'_{MC}), considering the interstitial velocity of the microchannel, defined by $U_{i_{MC}} = Q/(W_c H)$, leading to $k'_{MC} = 2.7 \times 10^{-10}\text{m}^2$.

Sands with non-spherical particles and different grain sizes, separated using different sieves, were considered as possible candidates for being the core material of the packed bed column. The target was to determine which sand size had a modified permeability similar to that calculated for the microchannels. To estimate the modified permeability of these sands (k'_{PM}), we used the Carman–Kozeny equation (Eq. 5) (Rhodes 2008), suitable for laminar flow of Newtonian fluids through a randomly packed bed of non-spherical particles:

$$\frac{-\Delta P}{L} = 180\frac{\mu U}{x_{32}^2}\frac{(1-\varepsilon)^2}{\varepsilon^3}, \tag{5}$$

where x_{32} is Sauter's mean diameter, which represents the diameter of a sphere having the same surface to volume ratio as the non-spherical particles in question, and ε is the porosity of the sand (Holdich 2002). Thus, considering Eqs. 4 and 5, the modified permeability of a porous medium predicted by Carman–Kozeny is given by

$$k'_{PM} = \frac{1}{180}\left(\frac{x_{32}\varepsilon}{1-\varepsilon}\right)^2, \tag{6}$$

where use was made of the relation between the interstitial and superficial velocities in a porous medium, $U_{i_{PM}} = U/\varepsilon$.

Among all the particle sizes considered, we selected the sand shown in Fig. 7, having an average particle size of $x_{32} = 400$ μm with a standard deviation of 90 μm, as measured by low angle forward light scattering (LS^{TM} 230 Laser Diffraction Particle Size Analyzer, Beckman Coulter Inc.). The porosity of this sand bed was $\varepsilon = 0.36 \pm 0.01$. The modified permeability of this sand was calculated by Eq. 6, resulting in $k'_{PM} = 2.8 \times 10^{-10}\text{m}^2$, corresponding to a relative deviation with regard to the modified permeability calculated for the microchannels (k'_{MC}) below 5%.

In this way, it has been confirmed that both microfluidic systems exhibit a similar modified permeability and are good analogues of a real porous medium when a Newtonian fluid is used.

3 Results and discussion

3.1 Pressure losses

Experiments with de-ionized water and aqueous polymer solutions were done in the sand beds with $x_{32} = 400$ μm. Figure 8 shows a comparison between the pressure gradient curves as a function of the flow rate, measured for the de-ionized water and both PAA solutions. At low flow rates, the polymer solutions behave as Newtonian fluids flowing through the porous medium, i.e. the flow is dominated by the viscous forces. As expected, in this region the addition of polymer enhances the pressure gradient, as a direct consequence of having a higher viscosity (Einstein 1906). Moreover, at these low flow rates both viscoelastic fluids exhibit similar slopes (ratio ≈ 1.18), since for such low shear rate range both fluids possess similar shear viscosities (Fig. 1), considering the experimental uncertainty (vertical error bars). For higher flow rates, and in spite of a reduction in viscosity associated with the shear-thinning

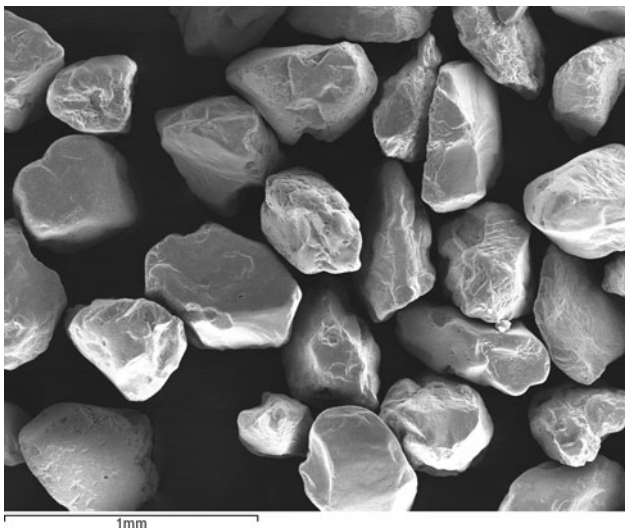

Fig. 7 SEM image of the sand used in the experiments, consisting of non-spherical particles with a Sauter mean diameter of $x_{32} = 400$ μm

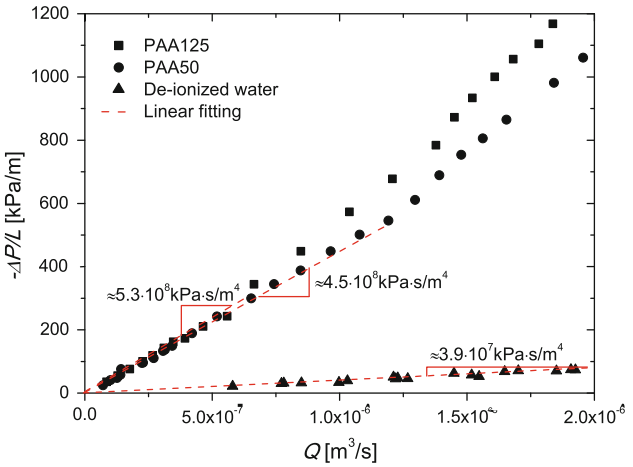

Fig. 8 Pressure gradient curves as a function of flow rate for the viscoelastic fluids and the Newtonian fluid (de-ionized water) for the flow in the porous media. *Dashed lines* represent the linear fittings to the Newtonian-like behavior

nature of the polymer solutions, we observe an increase in the slope of the pressure gradient curves for the viscoelastic fluids as the polymer chains unravel and elastic effects are manifested (Rodd et al. 2005). As expected, the elastic effects are observed at an earlier stage and in a more prominent way for the more concentrated polymer solution.

To assess the usefulness of the microfluidic devices to mimic the flow of viscoelastic fluids through a porous medium, the pressure gradient in the microchannels was also measured using the PAA solutions. Figure 9 shows the pressure gradient curves for the PAA solutions as a function of the Deborah number (*De*), which for an isotropic porous medium, can be calculated as

$$De = \lambda \frac{v}{l}, \tag{7}$$

where λ is the longest relaxation time measured in the CaBER for the fresh sample, l is a characteristic length scale (usually taken as the particle size) and v is a characteristic velocity (Marshall and Metzner 1967). The Deborah number represents a ratio of time scales of the material (λ) and of the flow process (l/v), allowing us to compare the results obtained in the microchannels with those obtained with the sand bed. To calculate the Deborah number in the porous medium corresponding to the sand bed experiments in a meaningful way, we used the interstitial velocity ($U_{\text{int}} = U/\varepsilon$) as the characteristic velocity, and Sauter's mean diameter ($x_{32} \approx 400$ μm) as the characteristic length scale for the porous media. For the microchannels, we used the velocity in the contraction sections ($U_{i_{\text{MC}}} = \frac{Q}{W_c H}$) as the characteristic velocity, while for the characteristic length scale we used the equivalent particle size ($d_{p_{\text{MC}}} \approx 390$μm), which was calculated using Eq. 6 considering the porosity of the selected sand to which the microchannels are equivalent ($\varepsilon = 0.36$) and the equivalent permeability of the microchannels ($k'_{\text{MC}} = 2.7 \times 10^{-10}\,\text{m}^2$).

In Fig. 9 it can be seen that, as the velocity is increased (and consequently *De*), the pressure gradient curve for the asymmetric microchannel is progressively above the curve for the symmetric channel. This enhanced pressure gradient is due to two simultaneous effects:

1. The value of the Deborah number ($De = \lambda \frac{U_i}{d_{p_{\text{MC}}}} = \lambda \frac{Q}{W_c H d_{p_{\text{MC}}}}$) for the asymmetric arrangement is smaller than for the symmetric geometry at the same flow rate, because of the larger W_c, which leads to a larger slope in the curve, since identical flow rates in both microfluidic arrangements leads to not too dissimilar pressure gradients.
2. It is currently widely accepted that the underlying mechanism for the onset of purely elastic flow instabilities is related to streamline curvature, and the development of large hoop stresses, which generates tension along fluid streamlines leading to flow destabilization (Larson et al. 1990; Pakdel and McKinley 1996; McKinley et al. 1996; Soulages et al. 2009). Pakdel and McKinley (1996, 1998) showed that the critical conditions for the onset of purely elastic instabilities can be described for a wide range of flows by a single dimensionless parameter (M), which accounts for elastic normal stresses and streamline curvature:

$$M = \sqrt{\frac{\lambda v}{\Re} \frac{\tau_{11}}{\tau_{12}}}, \tag{8}$$

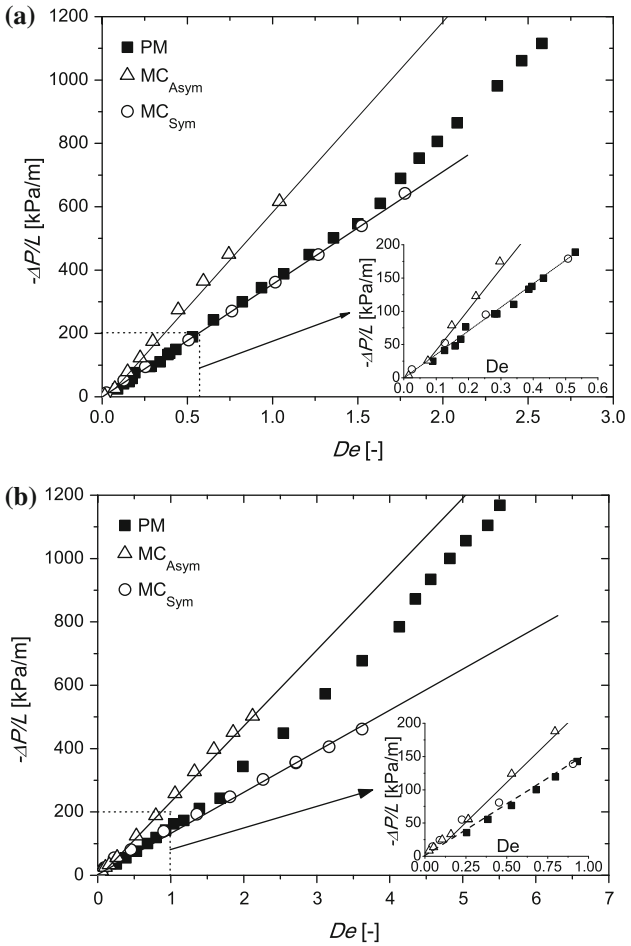

Fig. 9 Pressure gradient as a function of the Deborah number for the flow of the viscoelastic fluids through the asymmetric (MC_{Asym}) and symmetric (MC_{Sym}) microchannels, and through the porous medium (PM): **a** PAA50; **b** PAA125

where λ is the relaxation time of the fluid, v is the local streamwise fluid velocity, τ_{11} is the local tensile stress in the flow direction, τ_{12} is the shear stress ($\tau_{12} = \eta\dot{\gamma}$) and $\Re$ is the streamline local radius of curvature. This mechanism for the onset of purely elastic instabilities and the applicability of the M parameter to identify the critical conditions for the onset of elastic instabilities was confirmed numerically by Alves and Poole (2007) for creeping flow of UCM fluids in smooth contractions, for a wide range of contraction ratios. According to this argument, and since the asymmetric configuration presents more marked streamline curvatures, it is expected that there would be an extra contribution to the pressure gradient. Since the onset of elastic instabilities occurs at lower De in the asymmetric than in the symmetric configuration, as will be shown in the next section, this is indirect evidence for the higher $\Delta P/L$ versus De slope observed for the asymmetric microchannel.

This analysis is further corroborated in Fig. 9, where the inset graphs show that, at very low flow rates, both microchannels and the real porous medium exhibit similar Newtonian-limit behavior. This is a consequence of either the small magnitude or absence of elastic effects taking place at low flow rates. Moreover, it is also worth noting that the curve obtained for the real porous medium lies between those obtained for the microchannels. In real porous media, there indeed exists a critical value for the Deborah number (De_{cr}) above which the pressure gradient rises significantly due to elastic effects that also grow with the flow rate (Sousa et al. 2010; Rodd et al. 2005; Groisman et al. 2003). For the PAA solutions here considered this critical value is $De \approx 1.6$, as it is clear from Fig. 9, where a sudden change of slope is seen to take place for the flow in the porous medium.

The real porous medium is in practice, a complex combination of the two arrangements of particles simulated with the microchannels, which can be considered as limiting ideal configurations as sketched in Fig. 3. The results show that the symmetric microchannel describes better the viscoelastic fluid flow through a porous medium at low De values (between the end of the Newtonian-like behavior and the critical flow rate) than the asymmetric configuration. However, extrapolating the results to higher values of De, beyond those achieved here, it seems that the asymmetric configuration would be a more suitable description of the real porous medium.

For a better insight about the main factor responsible for the different pressure gradient profiles observed in the microchannels and for the rise-up in the slope of the pressure-gradient variation in the porous medium, we discuss the results of the flow visualizations in the microfluidic analogues in the following section.

3.2 Flow visualizations

The results of the flow visualizations are presented in Figs. 10 and 11 for the asymmetric and symmetric microchannels, respectively.

By flowing de-ionized water through the microchannels, small Moffatt vortices (Moffatt 1964) can be observed near the downstream corners at low flow rates (Figs. 10a, 11a). This is in agreement with the numerical predictions of Oliveira et al. (2008) for Newtonian fluids in two-dimensional flows at low Reynolds numbers. However, in microfluidic geometries given the small depth of the channels, the secondary flow is partially suppressed. Increasing the flow rate ($Re > 10$) leads to growing vortices downstream of the expansion plane (Figs. 10b, c for the asymmetric channel and 11b, c for the symmetric channel). A similar behavior was observed in previous studies

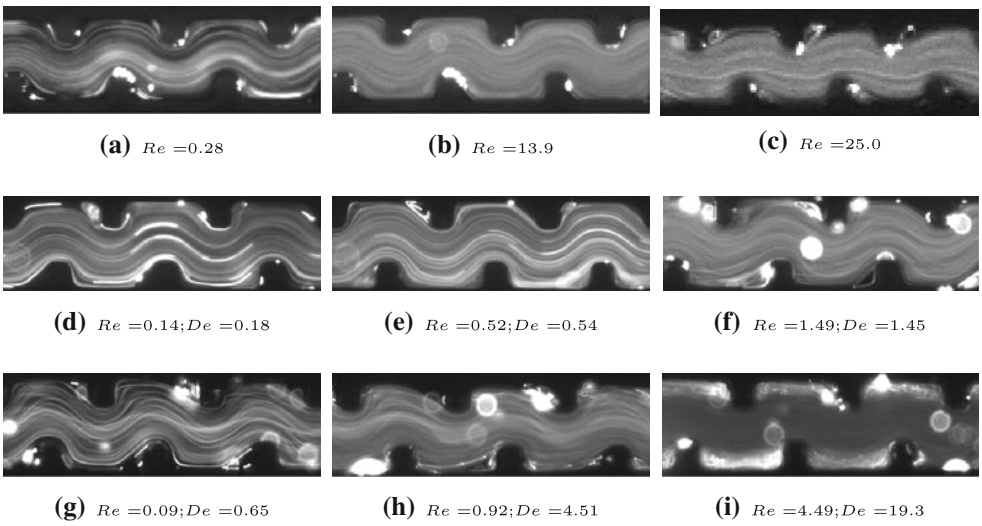

Fig. 10 Visualization of flow patterns in the asymmetric channel of the de-ionized water (*top*), PAA50 (*middle*) and PAA125 (*bottom*) solutions for various flow rates. Flow is from *left* to *right*

for Newtonian fluids (Scott 2004; Rodd et al. 2007; Oliveira et al. 2008).

The trends observed experimentally are similar for both viscoelastic fluids. In the asymmetric arrangement, at very low flow rates, small Moffatt vortices are observed near the far corners and the flow is Newtonian-like (figures not shown here). As the flow rate is increased, vortices appear upstream of the contractions and grow significantly in size due to the elastic effects (Fig. 10d, e for PAA50 and g for PAA125). Vortex growth upstream of the contraction is well documented for viscoelastic fluids (Scott 2004; Rodd et al. 2007). By increasing the flow rate, these vortices upstream of the contraction keep growing but additionally inertial effects are also observed ($Re \geq 1$) and the small vortex downstream of the expansion increases in size (Fig. 10f for PAA50 and h for PAA125), until the two vortices eventually merge (Fig. 10i for the PAA125), occupying most of the cavity defined by the geometric configuration. In this case, the fluid flows mainly through the central part of the channel and the streamlines become progressively rectilinear as the flow rate is increased and the recirculations occupy the whole volume of the cavity.

In the case of the symmetric channel, a more diverse range of flow features is observed. At very low flow rates, the flow is converging and diverging as the fluid approaches the contraction and expansion planes, respectively. At these flow rates (not shown here), the viscous effects are dominant and the flow patterns are similar to those obtained with the Newtonian fluid (Fig. 11a), and within each element the flow is symmetrical relative to both x- and the y-axes. As the flow rate is increased, the flow remains symmetric relative to the x-axis and vortex growth

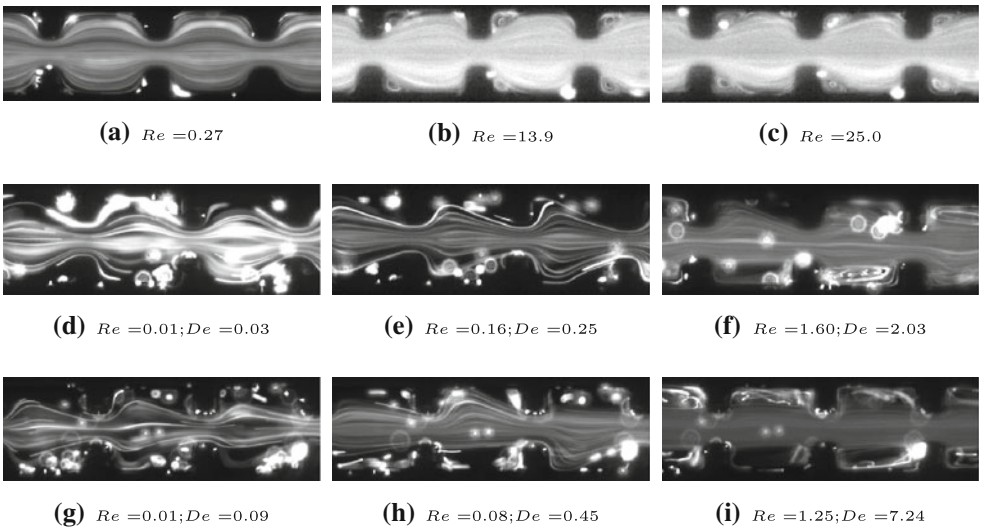

Fig. 11 Visualization of flow patterns in the symmetric channel of the de-ionized water (*top*), PAA50 (*middle*) and PAA125 (*bottom*) solutions for various flow rates. Flow is from *left* to *right*

upstream of the contraction is observed (Fig. 11d, e for PAA50 and g for PAA125). Eventually, for higher flow rates (which depends on the fluid used), the flow becomes asymmetric as highlighted in Fig. 11f (for PAA50) and h (for PAA125). Above a critical flow rate, the flow becomes unsteady due to the onset of elastic instabilities and the recirculations start growing and shrinking in certain elements in a complex pattern. There is also evidence of 3-D flow at the highest flow rates, as shown by the crossing of streamlines.

This analysis of the flow patterns supports the results obtained by pressure-gradient measurements (Fig. 9), which exhibit a slope of pressure gradient curves for the asymmetric microchannels above the ones measured for the symmetric configuration. The asymmetric microchannel magnifies the elastic effects as a consequence of higher streamline curvature and, therefore, the onset of the rise in the pressure gradient curve occurs at lower flow rates ($De < 0.5$). In the case of the symmetric microchannel, the streamlines are not so winding as in the asymmetric configuration and this elastic effect is reduced. We note, however, that elastic effects are also important for this symmetric configuration, otherwise the slope of the pressure gradient would decrease as De increases due to the shear-thinning rheology of the polymer solutions. As such, we argue that in the symmetric configuration the constant slope of the pressure gradient curve is a consequence of the balance between the decrease produced by shear thinning, and the increase induced by the elastic effects. Moreover, the appearance of the vortices occurs at higher flow rates in the case of the asymmetric arrangement, which is a consequence of having a larger W_c and its double effect, namely a reduction of shear rate ($\dot{\gamma}$) and corresponding De values. Therefore, these images seem to suggest that there is a unique pressure gradient slope (Fig. 9) for the symmetric arrangement, with shear thinning and extensional thickening competing approximately with the same intensity, thus leading to opposite contributions to the pressure gradient curve.

It is particularly useful to build up a De–Re flow pattern map, as shown in Fig. 12, highlighting the different flow patterns observed. The Reynolds number is defined as

$$Re = \frac{\rho U_{i_{MC}} W_c}{\eta}, \tag{9}$$

where ρ is the density and η is the shear viscosity of the fluid. Since the PAA fluids exhibit shear thinning behavior, η varies with the flow rate imposed in the experiment. A characteristic shear rate value ($\dot{\gamma} = \frac{U_{i_{MC}}}{W_c/2} = \frac{2Q}{W_c^2 H}$) was considered to determine the shear viscosity value from the flow curve (Fig. 1). Figure 12 shows that as the elasticity of the fluid increases (higher slope), the range of

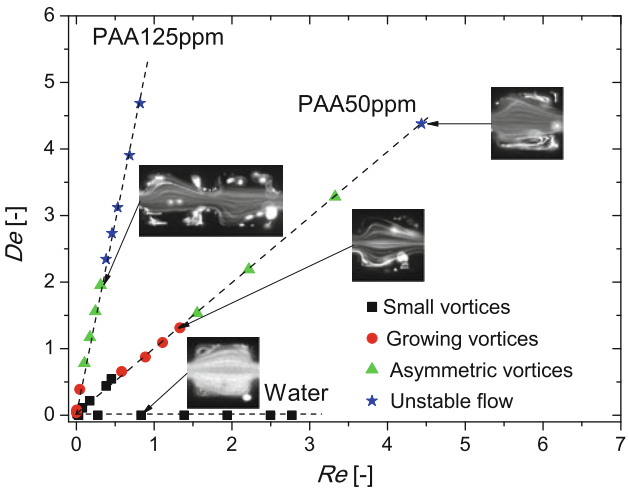

Fig. 12 De–Re flow pattern map for symmetric microchannels

De–Re conditions for which small vortices are present decreases and nearly vanishes for the PAA125 fluid. Small vortices are followed by a symmetric vortex growth regime and an asymmetric vortex growth region when the Deborah number is further increased. Eventually, the flow becomes unstable at higher De. However, it can be seen that the flow transitions of the PAA125 fluid occur at lower flow rates since the PAA125 fluid has a relaxation time significantly larger than the relaxation time of the PAA50 fluid. This indicates that elastic effects are present in a greater extent at the same inertial flow conditions for the PAA125 fluid. The reduction of the elasticity number ($El = De/Re$) with Re occurs due to shear thinning of the shear viscosity. At very low Reynolds numbers, the elasticity number of the PAA125 fluid is significantly larger than for the other fluid. A high elasticity number means that inertial effects are negligible compared to elastic effects. Therefore, vortex growth and elastic effects are already observed at very low Reynolds numbers for the PAA125 fluid, leading to an effective way of separating elastic effects from inertia-driven effects in the more concentrated fluid.

4 Conclusions

In this work, we have shown that microfluidic devices with special geometrical configurations can be used to study viscoelastic flow phenomena of aqueous polymer solutions occurring in porous media, but more than one geometric configuration may be required to represent the behavior in a wide range of flow rates. In our investigations, we used microchannels consisting of a sequence of contractions/expansions disposed in symmetrical and asymmetrical arrangements, which have been fabricated by soft lithography techniques. Both microchannels are shown to be

good porous medium analogues, despite their geometrical simplicity, as revealed by the good agreement in the pressure gradient results with the equivalent porous medium measurements for Newtonian liquids.

Additionally, the validity of these porous medium analogues for viscoelastic fluids has also been assessed. Due to the intrinsic differences in the extensional rate profiles defined by each microgeometry, the symmetric configuration is found to be more suitable for studying the flow of viscoelastic fluids at low *De* values, while the asymmetric microchannel gives better results at flow rates above the critical *De*. In this way, both microgeometries seem to be complementary and are very interesting tools to study the flow of viscoelastic fluids through a porous medium, as a result of the advantages associated with the use of optical techniques.

Acknowledgments Authors acknowledge financial support from Fundação para a Ciência e a Tecnologia (FCT), COMPETE and FEDER through projects PTDC/EQU-FTT/71800/2006, REEQ/262/EME/2005 and PTDC/EME-MFE/99109/2008. SEM images were taken at CEMUP, which is grateful for the financial support to FCT through projects REEQ/1062/CTM/2005 and REDE/1512/RME/2005. The technical support of L.C. Matos is also acknowledged. F.J. Galindo-Rosales would like to acknowledge FCT for financial support (SFRH/BPD/69663/2010). M.A. Alves acknowledges the Chemical Engineering Department of FEUP for conceding a sabbatical leave.

References

Alves MA, Poole RJ (2007) Divergent flow in contractions. J Non-Newton Fluid Mech 144:140–148

Balhoff MT, Thompson KE (2004) Modeling the steady flow of yield-stress fluids in packed beds. AIChE J 50(12):3034–3048

Blunt MJ (2001) Flow in porous media - pore-network models and multiphase flow. Curr Opin Colloid Interface Sci 6:197–207

Campo-Deaño L, Clasen C (2010) The slow retraction method (SRM) for the determination of ultra-short relaxation times in capillary breakup extensional rheometry experiments. J Non-Newton Fluid Mech 165:1688–1699

Chhabra RP, Comiti J, Machac I (2001) Flow of non-Newtononian fluids in fixed and fluidised beds. Chem Eng Sci 56:1–27

Christopher RH, Middleman S (1965) Power-law flow through a packed tube. Ind Eng Chem Fundam 4(4):422–426

Darcy H (1856) Les fountains publiques de la Ville de Dijon: exposition et application des principes à suivre et des formules à employer dans les questions de distribution d'eau. Victor Dalmont, Paris

Devasenathipathy S, Santiago JG, Wereley ST, Meinhart CD, Takehara K (2003) Particle imaging techniques for microfabricated fluidic systems. Exp Fluids 34:504514

Duda JL, Hong SA, Klaus EE (1983) Flow of polymer solutions in porous media: Inadequacy of the capillary model. Ind Eng Chem Fundam 22:299–305

Einstein A (1906) Eine neue Bestimmung der Moleküldimensionen. Annalen der Physik 19:298–306

Entov VM, Hinch EJ (1997) Effect of a spectrum of relaxation times on the capillary thinning of a filament of elastic liquid. J Colloid Interface Sci 72(1):31–51

Gaitonde NY, Middleman S (1966) Flow of viscoelastic fluids through porous media. Ind Eng Chem Fundam 6(1):145–147

Groisman A, Enzelberger M, Quake SR (2003) Microfluidic Memory and Control Devices. Science 300:955–958

Holdich R (2002) Fundamentals of particle technology. Midland Information Technology and Publishing, Loughborough

Larson RG, Shaqfeh ESG, Muller SJ (1990) A purely elastic instability in Taylor-Couette flow. J Non-Newton Fluid Mech 218:573–600

Liu Y, Wu SP (2009) Numerical simulations of non-Newtonian viscoelastic flows through porous media, in: Flow in porous media—from phenomena to engineering and beyond, Orient ACAD Forum, Marrickville, Australia, pp 187–193

López X (2004) Pore-Scale modelling of non-Newtonian flow. PhD thesis. Imperial College London

Macosko CW (1994) Rheology: principles, measurements, and applications. Wiley-VCH, Inc, New York

Marshall RJ, Metzner AB (1967) Flow of viscoelastic fluids through porous media. Ind Eng Chem Fundam 6(3):393–400

Martins A, Laranjeira PE, Braga CH, Mata TM (2009) Progress in Porous Media Research. Chapter 5: Modeling of transport phenomena in porous media using networks models. Nova Science Publishers, Inc, New York

McDonald JC, Dufy DC, Anderson JR, Chiu DT, Wu H, Whitesides GM (2000) Fabrication of microfluidic systems in poly(dimethylsiloxane). Electrophoresis 21:27–40

McKinley GH, Pakdel P, Oztekin A (1996) Rheological and geometric scaling of purely elastic flow instabilities. J Non-Newton Fluid Mech 67:19–47

Meinhart CD, Wereley ST, Gray MHB (2000) Volume illumination for two-dimensional particle image velocimetry. Meas Sci Technol 11:809–814

Metzner AB, Metzner AP (1970) Stress levels in rapid extensional flows of polymeric fluids. Rheol Acta 9(2):174–181

Moffatt HK (1964) Viscous and resistive eddies near sharp corners. J Fluid Mech 18(1):l–18

Oliveira MSN, Alves MA, Pinho FT, McKinley GH (2007) Viscous flow through microfabricated hyperbolic contractions. Exp Fluids 43:437–451

Oliveira MSN, Rodd LE, McKinley GH, Alves MA (2008) Simulations of extensional flow in microrheometric devices. Microfluid Nanofluid 5:809–826

Pakdel P, McKinley GH (1996) Elastic instability and curved streamlines. Phys Rev Lett 77:2459–462

Pakdel P, McKinley GH (1998) Cavity flows of elastic liquids: purely elastic instabilities. Phys Fluids 10(5):1058–1070

Pearson JRA, Tardy PMJ (2002) Models for flow of non-Newtonian and complex fluids through porous media. J Non-Newton Fluid Mech 102(2):447–473

Petrie CJS (2006a) Extensional viscosity: a critical discussion. J Non-Newton Fluid Mech 137:15–23

Petrie CJS (2006b) One hundred years of extensional flow. J Non-Newton Fluid Mech 137:1–14

Rhodes M (2008) Introduction to particle technology. 2nd edn. John Wiley & Sons, Ltd, England

Rodd LE, Cooper-White JJ, Boger DV, McKinley GH (2007) The role of elasticity number in the entry flow of dilute polymer solutions in micro-fabricated contraction geometries. J Non-Newton Fluid Mech 143:170–191

Rodd LE, Scott TP, Boger DV, Cooper-White JJ, McKinley GH (2005) The inertio-elastic planar entry flow of low-viscosity elastic fluids in micro-fabricated geometries. J Non-Newton Fluid Mech 129:1–22

Santiago JG, Wereley ST, Meinhart C, Beebe DJ, Adrian RJ (1998) A particle image velocimetry system for microfluidics. Exp Fluids 25:316–319

Savins JG (1969) Non-Newtonian flow through porous media. Ind Eng Chem 61(10):18–47

Scott TP (2004) Contraction/Expansion flow of dilute elastic solutions in Microchannels. Master's thesis. Massachusetts Institute of Technology

Sdougos HP, Bussolari SR, Dewey CF (1984) Secondary flow and turbulence in a cone-and-plate device. J Fluid Mech 138: 379–404

Sinton D (2004) Microscale flow visualization. Microfluid Nanofluid 1(1):2–21

Sochi T (2007) Pore-Scale modeling of non-Newtonian flow in porous media. PhD thesis. Imperial College London

Sochi T (2009) Pore-scale modeling of viscoelastic flow in porous media using a Bautista-Manero fluid. Int J Heat Fluid Flow 30:1202–1217

Sochi T (2010) Flow of non-Newtonian fluids in porous media. J Polymer Sci Part B Polymer Phys 48:2437–2467

Sorbie KS, Clifford PJ, Jones ERW (1989) The rheology of pseudo-plastic fluids in porous media using network modeling. J Colloid Interface Sci 130(2):508–534

Soulages J, Oliveira MSN, Sousa PC, Alves MA, McKinley GH (2009) Investigating the stability of viscoelastic stagnation flows in T-shaped microchannels. J Non-Newton Fluid Mech 163:9–24

Sousa PC, Pinho FT, Oliveira MSN, Alves MA (2010) Efficient microfluidic rectifiers for viscoelastic fluid flow. J Non-Newton Fluid Mech 165:652–671

Stone HA, Stroock AD, Ajdari A (2004) Engineering flows in small devices: microfluidics toward a lab-on-a-chip. Annu Rev Fluid Mech 36:381411

Taylor KC, Nasr-El-Din HA (1998) Water-soluble hydrophobically associating polymers for improved oil recovery: a literature review. J Petroleum Sci Eng 19:265–280

Whitesides GM (2006) The origins and future of microfluidics. Nature 42:368–370

Wissler EH (1971) Viscoelastic effects in the flow of non-Newtonian fluids through a porous medium. Ind Eng Chem Fundam 10(3):411–417